APL Materials

Adsorption-controlled growth of La-doped $BaSnO_3$ by molecular-beam epitaxy

Cite as: APL Mater. **5**, 116107 (2017); https://doi.org/10.1063/1.5001839
Submitted: 27 August 2017 • Accepted: 27 October 2017 • Published Online: 28 November 2017

Hanjong Paik, Zhen Chen, Edward Lochocki, et al.

ARTICLES YOU MAY BE INTERESTED IN

High-mobility $BaSnO_3$ grown by oxide molecular beam epitaxy
APL Materials **4**, 016106 (2016); https://doi.org/10.1063/1.4939657

Epitaxial integration of high-mobility La-doped $BaSnO_3$ thin films with silicon
APL Materials **7**, 022520 (2019); https://doi.org/10.1063/1.5054810

All-perovskite transparent high mobility field effect using epitaxial $BaSnO_3$ and $LaInO_3$
APL Materials **3**, 036101 (2015); https://doi.org/10.1063/1.4913587

© 2017 Author(s).

APL MATERIALS 5, 116107 (2017)

Adsorption-controlled growth of La-doped $BaSnO_3$ by molecular-beam epitaxy

Hanjong Paik,[1] Zhen Chen,[2] Edward Lochocki,[3] Ariel Seidner H.,[1] Amit Verma,[4] Nicholas Tanen,[1,5] Jisung Park,[1] Masaki Uchida,[6] ShunLi Shang,[7] Bi-Cheng Zhou,[7] Mario Brützam,[8] Reinhard Uecker,[8] Zi-Kui Liu,[7] Debdeep Jena,[1,5] Kyle M. Shen,[3,9] David A. Muller,[2,9] and Darrell G. Schlom[1,9,a]

[1]*Department of Material Science and Engineering, Cornell University, Ithaca, New York 14853, USA*
[2]*School of Applied and Engineering Physics, Cornell University, Ithaca, New York 14853, USA*
[3]*Laboratory of Atomic and Solid State Physics, Department of Physics, Cornell University, Ithaca, New York 14853, USA*
[4]*Department of Electrical Engineering, IIT Kanpur, Kanpur 208016, India*
[5]*School of Electrical and Computer Engineering, Cornell University, Ithaca, New York 14853, USA*
[6]*Department of Applied Physics and Quantum-Phase Electronics Center (QPEC), University of Tokyo, Tokyo 113-8656, Japan*
[7]*Department of Materials Science and Engineering, The Pennsylvania State University, University Park, Pennsylvania 16802, USA*
[8]*Leibniz Institute for Crystal Growth, D-12489 Berlin, Germany*
[9]*Kavli Institute at Cornell for Nanoscale Science, Ithaca, New York 14853, USA*

(Received 27 August 2017; accepted 27 October 2017; published online 28 November 2017)

Epitaxial La-doped $BaSnO_3$ films were grown in an adsorption-controlled regime by molecular-beam epitaxy, where the excess volatile SnO_x desorbs from the film surface. A film grown on a (001) $DyScO_3$ substrate exhibited a mobility of 183 cm^2 V^{-1} s^{-1} at room temperature and 400 cm^2 V^{-1} s^{-1} at 10 K despite the high concentration (1.2 $\times$ 10^{11} cm^{-2}) of threading dislocations present. In comparison to other reports, we observe a much lower concentration of $(BaO)_2$ Ruddlesden-Popper crystallographic shear faults. This suggests that in addition to threading dislocations, other defects—possibly $(BaO)_2$ crystallographic shear defects or point defects—significantly reduce the electron mobility. © *2017 Author(s). All article content, except where otherwise noted, is licensed under a Creative Commons Attribution (CC BY) license (http://creativecommons.org/licenses/by/4.0/).* https://doi.org/10.1063/1.5001839

Transparent conducting oxides with high mobility are being studied in hopes of realizing high-performance transparent electronics.[1] La-doped $BaSnO_3$ has emerged as a material of interest in this arena due to its high mobility at room temperature, transparency, and stability. La-doped $BaSnO_3$ single crystals are reported to have mobilities as high as 320 cm^2 V^{-1} s^{-1} at room temperature at a mobile electron concentration of $n = 8 \times 10^{19}$ cm^{-3}.[2] Indeed, La-doped $BaSnO_3$ has a higher mobility than all mainstream semiconductors (Si, GaAs, GaN, etc.) at doping concentrations above about $n = 10^{19}$ cm^{-3}, where it is degenerately doped;[3] CdO is the only transparent semiconductor with higher mobility in this doping range.[4] Another advantage of $BaSnO_3$ is its excellent structural match to ferroelectric and antiferroelectric oxides with the perovskite structure, e.g., $Pb(Zr, Ti)O_3$. This could enable La-doped $BaSnO_3$ to serve as a high mobility channel for smart transistors[5] including ferroelectric field-effect transistors[6–16] and yield a subthreshold slope beating the 60 mV/decade Boltzmann limit of conventional field-effect transistors by fabricating negative capacitance field-effect transistors (NCFETs).[17,18]

[a]Author to whom correspondence should be addressed: schlom@cornell.edu

 © Author(s) 2017

Two major deficiencies of currently epitaxially grown La-doped $BaSnO_3$ films that impact the performance of field-effect devices are the following: (1) their mobility is significantly lower[2,3,19–24] than what has been demonstrated in La-doped $BaSnO_3$ single crystals[2,24,25] and (2) when doped below about 1×10^{19} cm^{-3}, they are no longer conductive.[2,3,19–24] This latter point also applies to La-doped $BaSnO_3$ single crystals.[2,24] Both of these issues relate to the presence of significant concentrations of defects. The low mobility has been attributed to the high density of threading dislocations in epitaxial $BaSnO_3$ films that arise because they are grown on substrates to which they are poorly lattice matched.[2,19–24] High concentrations of threading dislocations are known to limit the mobility of other semiconductors including Ge,[26] (In, Ga)As,[27] In(As, Sb),[28] SiGe,[29] and GaN.[30] Indeed the mobilities of epitaxial GaN and $BaSnO_3$ films with threading dislocation densities in the 10^{10}–10^{11} cm^{-2} range have been observed to scale with the square root of the mobile carrier concentration,[2,19,30] in agreement with theory.[26,30] In addition to the ability of dislocations to trap charge, nonstoichiometry, i.e., the ratio of (La + Ba):Sn deviating from 1 in La-doped $BaSnO_3$ films and the point defects it leads to, could also be responsible for the insulating behavior seen in lightly La-doped $BaSnO_3$ thin films. The inability to lightly dope La-doped $BaSnO_3$ layers is an obstacle to the fabrication of depletion-mode field-effect transistors.

The cutoff at about 1×10^{19} cm^{-3} in mobile electron concentration, below which doped films are insulating, is indicative of the concentration of electron traps in $BaSnO_3$ thin films. If nonstoichiometry is the root of the traps, then insulating behavior below a lanthanum concentration of 1×10^{19} cm^{-3} implies that the films deviate by 0.07% or more from being stoichiometric. This value is comparable to state-of-the-art stoichiometry control in the deposition of multicomponent films by physical vapor deposition methods.[31–39] A way to circumvent this limit is to exploit thermodynamics by entering an adsorption-controlled growth regime where the volatile constituents are provided in excess, but film composition is controlled automatically and locally through the volatility of those constituents to produce single-phase films.[40–49] Adsorption-control has been extensively used for the growth of oxides,[50–52] including, most recently, for the growth of epitaxial $BaSnO_3$ films utilizing metalorganic precursors.[53]

In this letter, we utilize adsorption-controlled growth with inorganic precursors to achieve La-doped $BaSnO_3$ thin films (1) with higher mobility and (2) that are conductive to lower carrier concentrations than have been reported to date. Room-temperature mobilities in excess of 150 cm^2 V^{-1} s^{-1}, the prior mobility record,[22] are achieved in fully relaxed La-doped $BaSnO_3$ thin films on substrates with mismatches ranging from −5.1% ($SrTiO_3$) to −2.3% ($PrScO_3$). Our result demonstrates that dislocations are not the only defect that limit the mobility in La-doped $BaSnO_3$ thin films and emphasizes the importance of precisely controlling film stoichiometry.

La-doped $BaSnO_3$ thin films were grown in a Veeco GEN10 MBE system from molecular beams emanating from separate effusion cells containing lanthanum (99.996% purity, Ames Lab), barium (99.99% purity, Sigma-Aldrich), and SnO_2 (99.996% purity, Alfa Aesar), respectively, in combination with a molecular beam of oxidant (the ∼10% ozone + oxygen output of a commercial ozone generator).[54] The fluxes emanating from the effusion cells were determined by a quartz crystal microbalance (QCM) before growth. To achieve the desired doping concentration, the lanthanum flux was adjusted from the temperature at which its flux was measured by the QCM to a lower temperature, where accurate QCM measurements are not possible, by extrapolating its flux using the known activation energy of the vapor pressure of lanthanum,[55] i.e., a linear extrapolation of a plot of lanthanum vapor pressure vs. $1/T$. According to vapor pressure calculations, multiple species evaporate from SnO_2 under our growth conditions, with the major species being SnO.[56] In Sec. S1 of the supplementary material, the calculated vapor pressure of species over solid SnO_2 is plotted at a fixed oxygen partial pressure of 7.6×10^{-7} Torr (10^{-9} atm). We used an excess of SnO_x-flux (above 9.0×10^{13} atoms cm^{-2} s^{-1}) during growth, which is approximately three times greater than the barium flux (3.0×10^{13} atoms cm^{-2} s^{-1}). The background pressure of the oxidant, 10% O_3 + O_2, was held at a constant ion gauge pressure of 7.0×10^{-7} Torr. All components—lanthanum, barium, SnO_x, and the 10% O_3 + O_2 oxidant—were co-supplied during film growth. A variety of perovskite substrates were used: (100) $SrTiO_3$, (001) $DyScO_3$, (110) $DyScO_3$, (110) $TbScO_3$, (110) $GdScO_3$, (110) $Nd_{0.5}Sm_{0.5}ScO_3$, (110) $NdScO_3$, and (110) $PrScO_3$.[57] These are all pseudocubic perovskite {100} surfaces and upon them the $BaSnO_3$ films grew with a cube-on-(pseudo)cube orientation

relationship. The substrate temperature was maintained between 830 and 850 °C, as measured by an optical pyrometer. To determine the optimal single-phase growth window, we used *in situ* reflection high-energy electron diffraction (RHEED) as described below. The RHEED intensity oscillation period was used to estimate the film thickness and growth rate. The film growth rate was about 0.3 Å/s.

The phase purity and structural perfection of the films were assessed using four-circle x-ray diffraction (XRD) utilizing Cu K_a radiation with a high-resolution diffractometer (Panalytical X'Pert Pro MRD with a PreFix hybrid 4×Ge 220 monochromator on the incident beam side and a triple axis/rocking curve attachment (Ge 220) on the diffracted beam side). The microstructure and defects in the film were studied by cross-sectional and plan-view high (low)-angle annular dark field scanning transmission electron microscopy (HAADF-STEM and LAADF-STEM) with an FEI Titan Themis with a probe aberration corrector at 300 kV. Temperature-dependent electrical transport and Hall effect were measured in a van der Pauw geometry made by wire bonding aluminum wires to gold contact pads on the corners of the film.

Figure 1 shows the calculated oxygen partial pressure (Po_2) vs. temperature (T) diagram for the Ba-Sn-O system with the tin partial pressure fixed at 7.6×10^{-8} Torr (10^{-10} atm). It is constructed using the calculation of phase diagrams (CALPHAD) method and first-principles calculations (see Sec. S2 of the supplementary material for additional details).[58] The reaction enthalpy (ΔH) values shown in Table I are used for the formation of $Ba_{n+1}Sn_nO_{3n+1}$ phases with $n = 1, 2, 3$, and 4. The result is the four regions of stable solid phases shown in Fig. 1: (I) BaO, (II) Ba_2SnO_4, (III) $BaSnO_3$, and (IV) SnO_2, where the volatile SnO_x gas phases are balanced with each solid phase. First-principles calculations indicate that there is no driving force to form $Ba_{n+1}Sn_nO_{3n+1}$ with $n > 2$;[59] hence, the phases of $Ba_{n+1}Sn_nO_{3n+1}$ with $n > 2$ are not shown in Fig. 1; they are all lumped into stability region II. Overlaid onto Fig. 1 are RHEED patterns of La-doped $BaSnO_3$ thin films grown on (001) $DyScO_3$ substrates at different growth conditions (oxidant pressure and temperature).

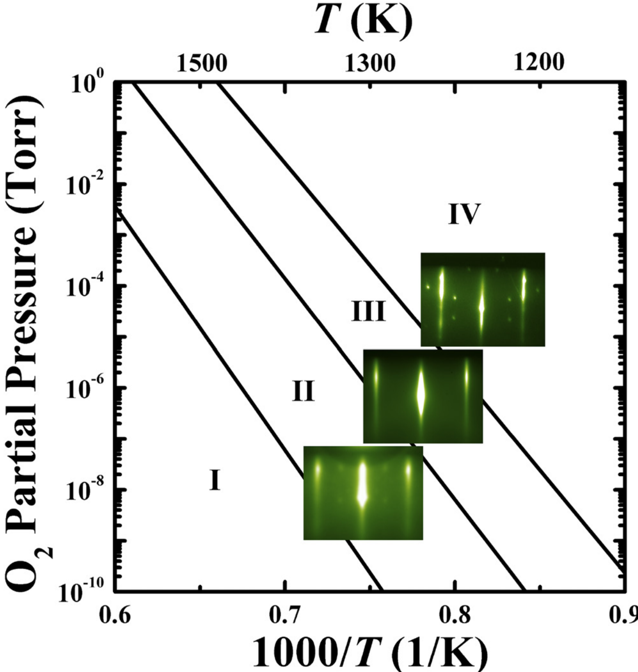

FIG. 1. Calculated Ellingham diagram (oxygen partial pressure vs. reciprocal temperature) with the tin partial pressure fixed at 7.6×10^{-8} Torr (10^{-10} atm) assuming an open system. The overlaid RHEED patterns are taken along the [110] $BaSnO_3$ azimuth from films grown on (001) $DyScO_3$ substrates at different substrate temperatures. The four regions of phase stability between SnO_x gases and the condensed phases are represented as (I) BaO, (II) Ba_2SnO_4, (III) $BaSnO_3$, and (IV) SnO_2, respectively, where the name of each region corresponds to the major condensed phase present. First-principles calculations, using the generalized gradient approximation (GGA) with Perdew-Burke-Ernzerhof revised for solids (PBEsol) functional, predicted the enthalpy of $BaSnO_3$ formation to be −107.5 kJ/mol per formula unit for the BaO + SnO_2 = $BaSnO_3$ reaction (see Table I).

TABLE I. Reaction enthalpy (ΔH) values for the formation of $Ba_{n+1}Sn_nO_{3n+1}$ phases with n = 1, 2, 3, and 4, calculated from first-principles with the PBEsol functional.

Reaction	ΔH (eV/atom)	ΔH (kJ/mol f.u.)
$BaO + SnO_2 = BaSnO_3$	−0.223	−107.5
$2BaO + SnO_2 = Ba_2SnO_4$	−0.228	−154.2
$3BaO + 2SnO_2 = Ba_3Sn_2O_7$	−0.227	−262.4
$4BaO + 3SnO_2 = Ba_4Sn_3O_{10}$	−0.225	−369.3

Within region III stoichiometric $BaSnO_3$ films grow free of any surface reconstruction, i.e., with a 1×1 RHEED pattern. This can be clearly seen in Fig. 2(a) from the sharp 1×1 LEED image of a La-doped $BaSnO_3$ film. In contrast, we observe a 2×1 RHEED pattern, with the $2\times$ reconstruction along the [110] azimuth of $BaSnO_3$ when the film growth conditions become slightly Ba-rich and move toward the boundary between region III and region II by either (1) increasing the substrate temperature, (2) lowering the flux supplied from the SnO_2 source, or (3) lowering the ozone partial pressure. Exiting region III and moving into region II are manifested by a more diffuse RHEED pattern with spots corresponding to the growth of a disordered Ruddlesden-Popper phase,[60–62] loaded with syntactic intergrowths of $Ba_{n+1}Sn_nO_{3n+1}$ layers with varying n. The θ-2θ XRD pattern of a sample film grown in region II exhibiting such intergrowth disorder is shown in Fig. S2 of the supplementary material. This pattern can be indexed as $Ba_8Sn_7O_{22}$. A hallmark of intergrowth disorder is the presence of both even and odd XRD indices;[63,64] an ideally ordered Ruddlesden-Popper

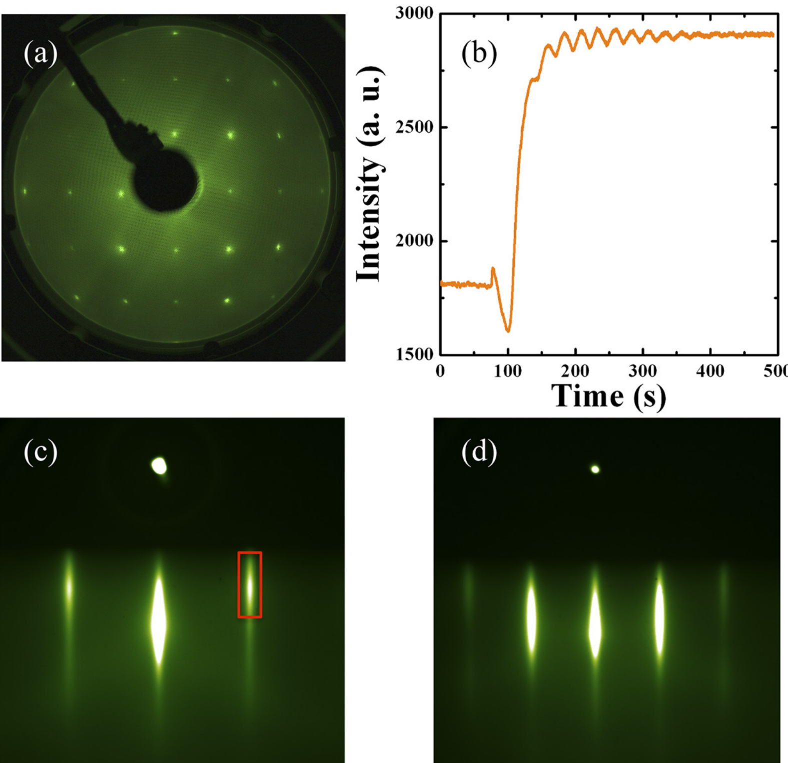

FIG. 2. (a) Low-energy electron diffraction (LEED) pattern of a 25-nm-thick, 3.5 at. % La-doped $BaSnO_3$ thin film grown on a (110) $TbScO_3$ substrate. (b) Reflection high-energy electron diffraction (RHEED) intensity oscillation during the growth of an undoped $BaSnO_3$ buffer layer on a (001) $DyScO_3$ substrate. RHEED images of a 60-nm-thick La-doped $BaSnO_3$ film with a mobile carrier concentration of 1.2×10^{20} cm^{-3} [grown on top of the 330-nm-thick undoped $BaSnO_3$ buffer layer shown in (b)] viewed along the (c) [110] and (d) [100] azimuths of $BaSnO_3$.

phase would contain only even XRD indices because of the presence of the glide plane perpendicular to the *c*-axis.

If, on the other hand, starting from region III the fluxes are made more Sn-rich or the substrate temperature is lowered, a transmission RHEED pattern indicative of rough, three-dimensional growth is observed along both the [110] and [100] azimuths of $BaSnO_3$. This is indicative of the accumulation of SnO_2 in the film as the growth moves into region IV. The rough SnO_2 phase gives rise to the spots in the resulting RHEED pattern; the streaks are from the perovskite $BaSnO_3$ phase. The resulting mixed-phase sample corresponds to SnO_2 + $BaSnO_3$ as shown by the XRD and RHEED results in Fig. S5 of the supplementary material. Alternatively, if one again starts in region III and increases the ozone pressure (leaving all other growth parameters constant), a three-dimensional transmission RHEED pattern indicative of condensed SnO_2 on the film surface is seen. All of these observed changes are fully consistent with the expectations implied by Fig. 1. The ability to see them *in situ* by RHEED allows one to reliably find the desired growth window (region III) for the adsorption-controlled growth of phase-pure $BaSnO_3$ thin films. For additional details, see Sec. S3 of the supplementary material.

Figure 2(b) shows RHEED intensity oscillations during the initial growth of a $BaSnO_3$ film on a (001) $DyScO_3$ substrate. The corresponding RHEED patterns of the same $BaSnO_3$ film along the [110] and [100] azimuths of $BaSnO_3$ are shown in Figs. 2(c) and 2(d), respectively.

The RHEED intensity oscillation was monitored at the off-specular position (marked by the red box) along the [110] azimuth of $BaSnO_3$ shown in Fig. 2(c). Initially the $BaSnO_3$ film grew in a layer-by-layer growth mode, but due to the large lattice mismatch (−4.2%) between the (001) $DyScO_3$ substrate (a_{DyScO_3}, pseudocubic = $\sqrt{\frac{ab}{2}}$ = 3.943 Å)[65] and $BaSnO_3$ film (a_{BaSnO_3} = 4.116 Å),[66] the film quickly relaxed and the amplitude of the RHEED oscillations decreased. Concomitant with this relaxation, the growth mode changed to step-flow after the growth of about 13-15 unit cells. The film growth rate was 0.3 Å/s (equivalently ∼0.1 µm/h), based on both the RHEED intensity oscillations and thickness fringes observed by XRD.

The same $BaSnO_3$ film characterized by RHEED in Figs. 2(b)–2(d)—a 60-nm-thick La-doped $BaSnO_3$ film with a mobile carrier concentration of 1.2×10^{20} cm^{-3} grown on a 330-nm-thick undoped $BaSnO_3$ buffer layer on a (001) $DyScO_3$ substrate—is characterized by XRD in Fig. 3.

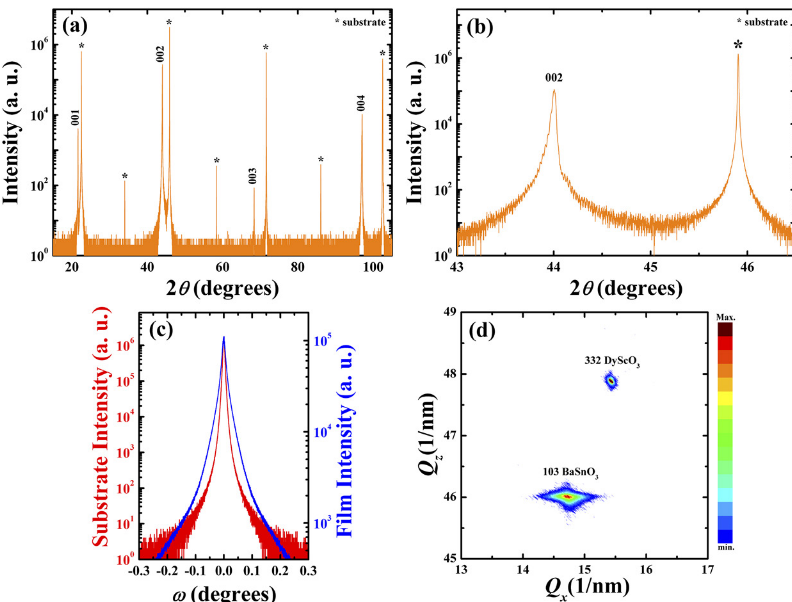

FIG. 3. XRD scans of a 60-nm-thick La-doped $BaSnO_3$ film grown on a 330-nm-thick undoped $BaSnO_3$ buffered layer on a (001) $DyScO_3$ substrate measured in a triple-axis geometry. (a) *θ*-2*θ* scan. (b) A close-up view of the *θ*-2*θ* scan around the 002 La-doped $BaSnO_3$ peak showing clear thickness fringes. The total thickness of the $BaSnO_3$ film is calculated to be 390 ± 0.2 nm. (c) Overlaid rocking curves of the 002 $BaSnO_3$ film peak and the 004 $DyScO_3$ substrate peak. (d) A reciprocal space map around the 103 $BaSnO_3$ film and the 332 $DyScO_3$ substrate peak. The substrate peaks are labeled with asterisks.

The θ-2θ scan is shown in Fig. 3(a). The total film thickness is calculated based on the Kiessig fringes[67] around the 002 Bragg peak of $BaSnO_3$, as shown in Fig. 3(b). The θ-2θ scan exhibits solely the 00ℓ reflections of $BaSnO_3$ without any impurity phase. From these reflections, the c-axis of this La-doped $BaSnO_3$ film is calculated to be $c = 4.116 \pm 0.001$ Å using a Nelson-Riley fit;[68] this is in agreement with the bulk lattice constant of $BaSnO_3$, $a = 4.116$ Å.[66] A comparison of the structural perfection of this same La-doped $BaSnO_3$ film and the underlying $DyScO_3$ substrate it was grown upon are shown in Fig. 3(c). Here, the rocking curve of the 002 peak of the La-doped $BaSnO_3$ film is overlaid upon the 004 peak of the $DyScO_3$ substrate. The full width at half maximum (FWHM) of the film peak is 0.016°, which is far broader than the 0.0062° FWHM of the substrate. Although narrower than all prior reported FWHM for as-grown $BaSnO_3$-based heterostructures,[3,19,20,23,24] this relatively broad rocking curve is consistent with structural relaxation by the introduction of dislocations during the growth of the thick and highly mismatched (−4.2%) La-doped $BaSnO_3$ film on (001) $DyScO_3$. A reciprocal space map of the 103 $BaSnO_3$ peak of this same film is shown in Fig. 3(d). The in-plane and out-of-plane lattice constants of this La-doped $BaSnO_3$ film were calculated to be 4.1161 ± 0.001 Å and 4.1163 ± 0.001 Å, respectively, indicating that the La-doped $BaSnO_3$ film is fully relaxed. An atomic force microscope image of this same film is shown in Sec. S4 of the supplementary material.

Figure 4 shows the temperature dependence of (a) resistivity, (b) carrier concentration, and (c) mobility of the same La-doped $BaSnO_3$ sample characterized in Figs. 2(b)–2(d) and 3. The resistivity at room temperature is $2.3 \times 10^{-4}\ \Omega$ cm and its temperature dependence exhibits metallic behavior down to 10 K with a resistivity ratio, ρ_{300K}/ρ_{10K}, of 2.15. The concentration of negatively charged mobile carriers (n) is temperature independent, as shown in Fig. 4(b). Assuming that all of the mobile

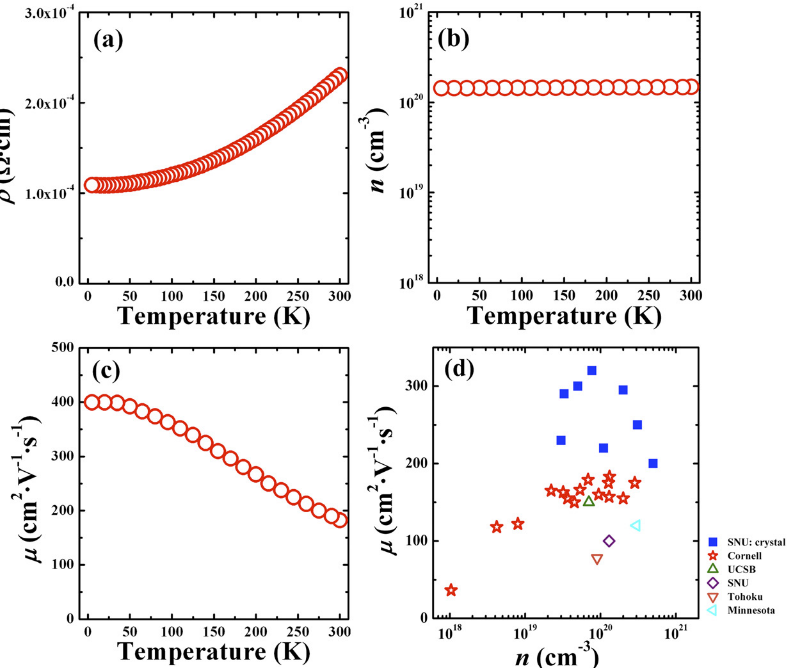

FIG. 4. (a) Resistivity vs. temperature, (b) mobile electron carrier concentration vs. temperature, and (c) electron mobility vs. temperature of the same La-doped $BaSnO_3$ film characterized in Figs. 2(b)–2(d) and 3. In (d) measurements of the mobility vs. mobile electron carrier concentration are made for a multitude of La-doped $BaSnO_3$ films grown on (100) $SrTiO_3$, (001) $DyScO_3$, (110) $DyScO_3$, (110) $TbScO_3$, (110) $GdScO_3$, (110) $Nd_{0.5}Sm_{0.5}ScO_3$, (110) $NdScO_3$, and (110) $PrScO_3$ substrates. All of the "Cornell" films were grown under the adsorption-controlled growth conditions described in this Letter. Also plotted for comparison are the highest mobility La-doped $BaSnO_3$ single crystals from Kim *et al.*[2] at Seoul National University (SNU, solid blue squares) and the highest mobility La-doped $BaSnO_3$ films from Raghavan *et al.*[22] at the University of California, Santa Barbara (UCSB, green triangle), Kim *et al.*[2,24] at SNU (purple diamond), Shiogai *et al.*[21] at Tohoku University (orange upside down triangle), and Prakash *et al.*[23] at the University of Minnesota (cyan sideways triangle).

carriers are attributable to the 60-nm-thick La-doped $BaSnO_3$ layer, the Hall resistance implies that n is 1.2×10^{20} cm^{-3}. The mobility (μ) of this same sample was 183 cm^2 V^{-1} s^{-1} at room temperature and reached 400 cm^2 V^{-1} s^{-1} at 10 K as can be seen in Fig. 4(c). This room-temperature mobility is 20% higher than the previous record, 150 cm^2 V^{-1} s^{-1}, which was achieved on a (110) $PrScO_3$ substrate.[22]

The sample described in detail so far is our highest mobility sample. The room-temperature mobility of other La-doped $BaSnO_3$ samples grown using the same adsorption-controlled growth conditions on a variety of substrates and with differing doping concentrations is shown in Fig. 4(d). These substrates ranged from $SrTiO_3$ to $PrScO_3$, with lattice matches to $BaSnO_3$ ranging from −5.1% to −2.3%, respectively. Note that the room-temperature mobility of La-doped $BaSnO_3$ films on all of these substrates was higher than 160 cm^2 V^{-1} s^{-1} for doping concentrations in the $(2–30) \times 10^{19}$ cm^{-3} range. Additionally, our growth conditions enable films with mobile carrier concentrations all the way down to 1×10^{18} cm^{-3} to be achieved;[69] this is an order of magnitude lower than prior reports.[2,3,19–24] The ability to dope $BaSnO_3$ at lower levels is consistent with the improved stoichiometry control that can accompany adsorption-controlled growth, leading to a reduction in the concentration of traps.

We investigated the defect structure of the La-doped $BaSnO_3$ sample with the highest mobility, the same sample whose other characteristics appear in Figs. 2–4, by STEM. A cross-sectional LAADF-STEM image of the entire film thickness is shown in Fig. 5(a). The high sensitivity of LAADF to strain and dislocations[70] makes it easy to see the threading dislocations. They are the vertically running defects with dark contrast in the $BaSnO_3$ film; one is indicated by a yellow arrow in Fig. 5(a). The HAADF-STEM images in Figs. 5(b) and 5(c) characterize the fully relaxed interface between the $DyScO_3$ substrate and the $BaSnO_3$ film. The spacing between the edge dislocations is on average 23 unit cells of $DyScO_3$ vs. 22 unit cells of $BaSnO_3$, which is consistent with that calculated from the ratio of the relaxed lattice parameters. Extended dislocations can also be seen, as indicated by the yellow arrow in Fig. 5(b).

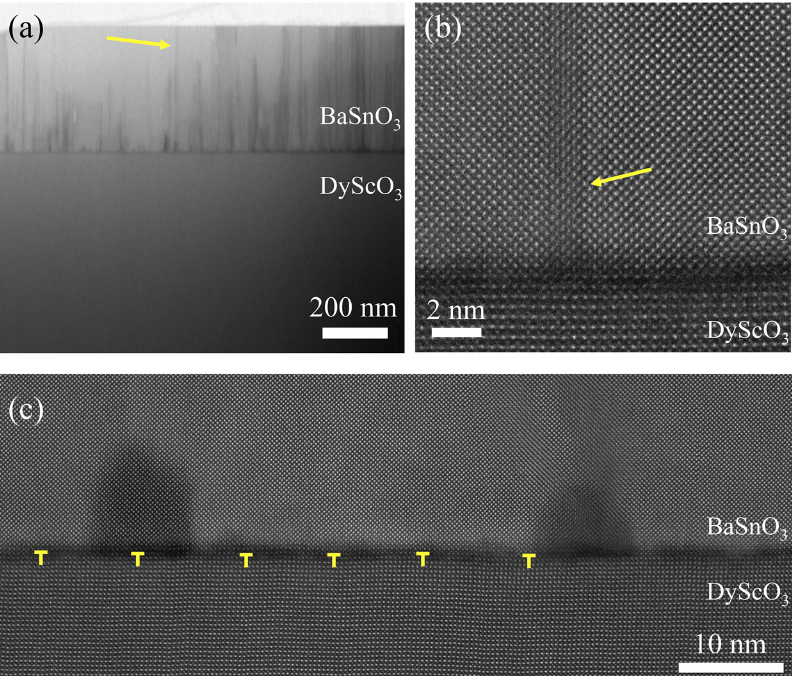

FIG. 5. Cross-sectional STEM images of the same La-doped $BaSnO_3$ film characterized in Figs. 2–4. (a) LAADF-STEM image showing the entire film thickness. The yellow arrow indicates a threading dislocation. HAADF-STEM images of the $BaSnO_3/DyScO_3$ interface are shown in (b) and (c). Edge dislocations are labeled in (c).

The density of threading dislocations in the same high-mobility sample characterized in Figs. 2–5 was determined by plan-view STEM measurements (Fig. 6) to be 1.2×10^{11} cm^{-2}. A high-resolution HAADF-STEM image is shown in Fig. 6(d) showing two partial edge dislocations, each with Burgers vectors having in-plane projections of ½ $\boldsymbol{a}$ ⟨110⟩. A full dislocation with a Burgers vector having an in-plane projection of $\boldsymbol{a}$ ⟨110⟩ is shown in Sec. S5 of the supplementary material.

Interestingly, some of these dislocations have hollow cores. Being devoid of atoms, the hollow cores appear black in the plan-view HAADF-STEM images in Fig. 6(d) and Fig. S7 of the supplementary material. The magnitude of the smallest Burgers vector having an energetically stable hollow core lies in the range $20\pi\frac{\gamma}{\mu}$ to $40\,\pi\sqrt{e}\frac{\gamma}{\mu}$ for isotropic materials according to Frank's approximate theory,[71] where γ is the surface energy and μ is the shear modulus. Using the calculated value of the surface energy (1.5 J/m^2)[72] and the measured value of the shear modulus (99.9 GPa)[73] of $BaSnO_3$, Frank's estimate of the minimum magnitude of the Burgers vector for it to have a hollow core lies in the 9-30 Å range. The two neighboring dislocations with outlined Burgers circuits in Fig. 6(d) both have Burgers vectors with in-plane projections of ½ $\boldsymbol{a}$ ⟨110⟩, i.e., a magnitude of $\frac{a}{\sqrt{2}}$ or 2.91 Å, yet one is hollow and the other is not.

This could be because the out-of-plane components of the Burgers vectors of these two dislocations are not identical; they could have mixed character rather than being pure edge dislocations. Another possibility is that the adsorption-controlled growth conditions lead to excess SnO_x species on the film surface during growth, which acts as a flux that lowers γ.[71] The amount that γ is lowered

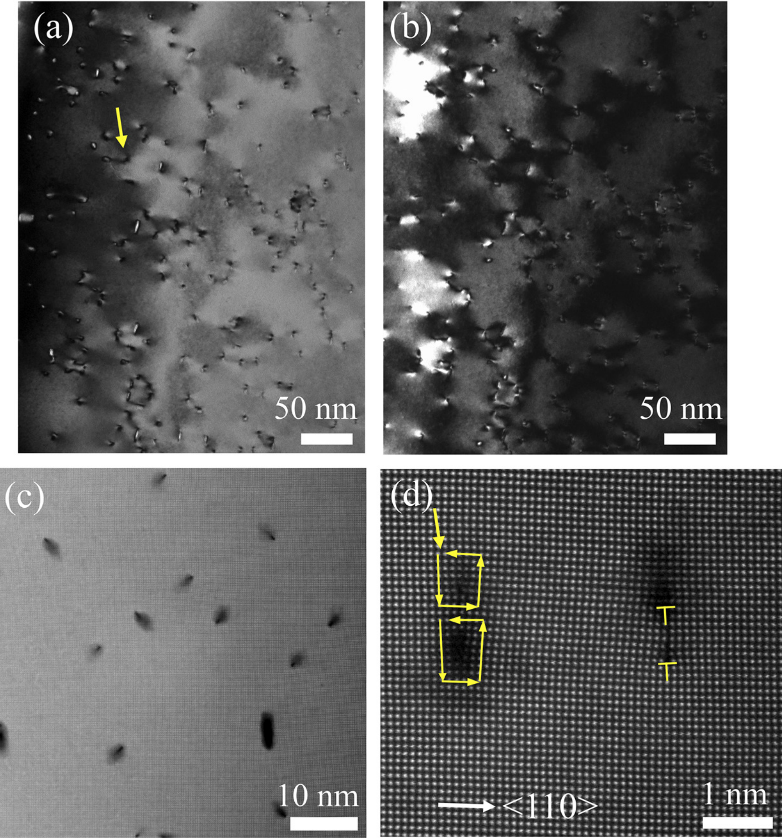

FIG. 6. Plan-view STEM images of the same La-doped $BaSnO_3$ film characterized in Figs. 2–5. (a) Bright-field and (b) dark-field STEM images. (c) and (d) are low and high magnification HAADF-STEM images, respectively. From these images, the density of threading dislocations is 1.2×10^{11} cm^{-2}. The yellow arrow in (a) shows a threading dislocation. Four dislocations are present in (d). The Burgers circuit is drawn for the two on the left, revealing two partial edge dislocations, each with a Burgers vector with an in-plane projection of ½ $\boldsymbol{a}$ ⟨110⟩. The dislocation that is arrowed is not hollow, whereas the dislocation below it is hollow.

depends on the concentration of flux and could vary spatially, leading to dislocations that are hollow or not hollow even though they have identical magnitudes of their Burgers vectors.

The huge density of dislocations observed in this film with record mobility (1.2×10^{11} cm^{-2}) led us to question if there might be some other defects besides dislocations that currently limit mobility in $BaSnO_3$ films. After all, our films are grown on the same substrates and have comparable dislocation densities to prior studies,[19] yet the mobilities are far higher. How is it that our films have higher mobility? We do not know the answer to this question and are studying it further; what little we do know is mentioned below.

A potential culprit is Ruddlesden-Popper[60–62] $(BaO)_2$ crystallographic shear defects, which have been reported to be a dominant structural defect in La-doped $BaSnO_3$ films grown by pulsed-laser deposition.[74] The TEM images in the study of Wang *et al.*[74] reveal a concentration of $(BaO)_2$ crystallographic shear defects of about 2×10^{11} cm^{-2}. In contrast, we see far fewer. We observed only one loop-shaped stacking fault in our highest mobility film (see Sec. S6 of the supplementary material). No stacking faults were observed in another two different areas with similar fields of view, leading us to estimate that the density of loop-shaped stacking faults in the film studied in Figs. 2–6 is about 3×10^9 cm^{-2}.

Differences in point defect concentrations could also be responsible for our films exhibiting higher mobility than other $BaSnO_3$ films with comparable dislocation densities. Vacancies on the barium site (V''_{Ba}) or on the tin site (V''''_{Sn}) are low-energy acceptor defects[75,76] in $BaSnO_3$ that could be responsible for the lack of conductivity in lightly La-doped $BaSnO_3$ films as well as the reduction in mobility when sufficient lanthanum is added to achieve conductivity.

The local and automatic composition control provided by thermodynamics under adsorption-controlled growth conditions could significantly reduce the concentration of V''_{Ba}, V''''_{Sn}, and other point defects, thus enhancing mobility. Note that adsorption-control is not synonymous with perfect composition control. Adsorption-control accesses the single-phase region of $BaSnO_3$, but depending on how wide that region is and from which side it is approached (in our case the SnO_x-rich side)—things that change with temperature and chemical potentials—the stoichiometry of the resulting film will change though it will always remain single phase. This is fully analogous to the growth of III-V compounds, where this behavior is well understood and utilized to controllably alter point defect concentrations, e.g., the EL2 defect in GaAs.[77]

In summary, using adsorption-controlled MBE growth, La-doped $BaSnO_3$ thin films with room-temperature mobilities as high as 183 cm^2 V^{-1} s^{-1} were achieved on highly mismatched substrates despite high concentrations ($\sim 10^{11}$ cm^{-2}) of threading dislocations. Further, this growth method enabled La-doped $BaSnO_3$ with mobile carrier concentrations as low as 1×10^{18} cm^{-3} to be achieved.[69] These results imply that threading dislocations are not the only defects that have been limiting the mobility and trapping carriers in La-doped $BaSnO_3$ thin films. Other defects, possibly $(BaO)_2$ crystallographic shear defects or point defects arising from nonstoichiometry, are potential culprits. These results make us believe that the combination of adsorption-controlled MBE with lattice-matched perovskite substrates will be a promising path to high-mobility La-doped $BaSnO_3$ thin films.

See supplementary material for additional details regarding the thermodynamic calculations as well as the structural and spectroscopic characterization of the $BaSnO_3$ films.

We gratefully acknowledge stimulating discussions with Karthik Krishnaswamy and Chris Van de Walle. This material is based upon work supported by the Air Force Office of Scientific Research under Award No. FA9550-16-1-0192 and by the National Science Foundation [Platform for the Accelerated Realization, Analysis, and Discovery of Interface Materials (PARADIM)] under Cooperative Agreement No. DMR-1539918. We also acknowledge support from the Center for Low Energy Systems Technology (LEAST), one of the six SRC STARnet Centers, sponsored by MARCO and DARPA. This work made use of the Cornell Center for Materials Research (CCMR) Shared Facilities, which are supported through the NSF MRSEC program (No. DMR-1719875). Substrate preparation was performed in part at the Cornell NanoScale Facility, a member of the National Nanotechnology Coordinated Infrastructure (NNCI), which is supported by the NSF (Grant No. ECCS-15420819).

[1] H. Hosono, Thin Solid Films **515**, 6000–6014 (2007).
[2] H. J. Kim, U. Kim, H. M. Kim, T. H. Kim, H. S. Mun, B.-G. Jeon, K. T. Hong, W.-J. Lee, C. Ju, K. H. Kim, and K. Char, Appl. Phys. Express **5**, 061102 (2012).
[3] U. Kim, "$BaSnO_3$: Thin film growth, transport properties, devices, and interfaces," Ph.D. thesis, Seoul National University, 2015, p. 15.
[4] E. Sachet, C. T. Shelton, J. S. Harris, B. E. Gaddy, D. L. Irving, S. Curtarolo, B. F. Donovan, P. E. Hopkins, P. A. Sharma, A. L. Sharma, J. Ihlefeld, S. Franzen, and J.-P. Maria, Nat. Mater. **14**, 414–420 (2015).
[5] Y. R. Wu and J. Singh, IEEE Trans. Electron Devices **52**, 284–293 (2005).
[6] D. H. Looney, U.S. patent No. 2,791,758 (7 May 1957).
[7] W. L. Brown, U.S. patent No. 2,791,759 (7 May 1957).
[8] I. M. Ross, U.S. patent No. 2,791,760 (7 May 1957).
[9] J. A. Morton, U.S. patent No. 2,791,761 (7 May 1957).
[10] J. L. Moll and Y. Tarui, IEEE Trans. Electron Devices **10**, 338–339 (1963).
[11] P. M. Heyman and G. H. Heilmeier, Proc. IEEE **54**, 842–848 (1966).
[12] G. G. Teather and L. Young, Solid-State Electron. **11**, 527–533 (1968).
[13] L. L. Chang and L. Esaki, IBM Tech. Discl. Bull. **14**, 1250–1251 (1971).
[14] S. Y. Wu, IEEE Trans. Electron Devices **21**, 499–504 (1974).
[15] S. L. Miller and P. J. McWhorter, J. Appl. Phys. **72**, 5999–6010 (1992).
[16] T. P. Ma and J.-P. Han, IEEE Electron Device Lett. **23**, 386–388 (2002).
[17] S. Salahuddin and S. Datta, Nano Lett. **8**, 405–410 (2008).
[18] A. I. Khan, K. Chatterjee, B. Wang, S. Drapcho, L. You, C. Serrao, S. R. Bakaul, R. Ramesh, and S. Salahuddin, Nat. Mater. **14**, 182–186 (2014).
[19] H. Mun, U. Kim, H. M. Kim, C. Park, T. H. Kim, H. J. Kim, K. H. Kim, and K. Char, Appl. Phys. Lett. **102**, 252105 (2013).
[20] U. Kim, C. Park, T. Ha, R. Kim, H. S. Mun, H. M. Kim, H. J. Kim, T. H. Kim, N. Kim, J. Yu, K. H. Kim, J. H. Kim, and K. Char, APL Mater. **2**, 056107 (2014).
[21] J. Shiogai, K. Nishihara, K. Sato, and A. Tsukazaki, AIP Adv. **6**, 065305 (2016).
[22] S. Raghavan, T. Schumann, H. Kim, J. Y. Zhang, T. A. Cain, and S. Stemmer, APL Mater. **4**, 016106 (2016).
[23] A. Prakash, P. Xu, A. Faghaninia, S. Shukla, J. W. Ager, C. S. Lo, and B. Jalan, Nat. Commun. **8**, 15167 (2017).
[24] H. J. Kim, U. Kim, T. H. Kim, J. Kim, H. M. Kim, B.-G. Jeon, W.-J. Lee, H. S. Mun, K. T. Hong, J. Yu, K. Char, and K. H. Kim, Phys. Rev. B **86**, 165205 (2012).
[25] Z. Galazka, R. Uecker, K. Irmscher, D. Klimm, R. Bertram, A. Kwasniewski, M. Naumann, R. Schewski, M. Pietsch, U. Juda, A. Fiedler, M. Albrecht, S. Ganschow, T. Markurt, C. Guguschev, and M. Bickermann, J. Phys.: Condens. Matter **29**, 075701 (2017).
[26] B. Pödör, Phys. Status Solidi B **16**, K167–K170 (1966).
[27] D. Zhao and K. J. Kuhn, IEEE Trans. Electron Devices **38**, 2582–2589 (1991).
[28] R. J. Egan, V. W. L. Chin, and T. L. Tansley, J. Appl. Phys. **75**, 2473–2476 (1994).
[29] R. M. Feenstra and M. A. Lutz, J. Appl. Phys. **78**, 6091–6097 (1995).
[30] H. M. Ng, D. Doppalapudi, T. D. Moustakas, N. G. Weimann, and L. F. Eastman, Appl. Phys. Lett. **73**, 821–823 (1998).
[31] M. E. Klausmeier-Brown, J. N. Eckstein, I. Bozovic, and G. F. Virshup, Appl. Phys. Lett. **60**, 657–659 (1992).
[32] S. J. Benerofe, C. H. Ahn, M. M. Wang, K. E. Kihlstrom, K. B. Do, S. B. Arnason, M. M. Fejer, T. H. Geballe, M. R. Beasley, and R. H. Hammond, J. Vac. Sci. Technol., B: Microelectron. Nanometer Struct. **12**, 1217–1220 (1994).
[33] C. Lu and Y. Guan, J. Vac. Sci. Technol., A **13**, 1797–1801 (1995).
[34] W. Wang, R. H. Hammond, M. M. Fejer, C. H. Ahn, M. R. Beasley, M. D. Levenson, and M. L. Bortz, Appl. Phys. Lett. **67**, 1375–1377 (1995).
[35] B. Utz, S. Rieder-Zecha, and H. Kinder, IEEE Trans. Appl. Supercond. **7**, 1181–1184 (1997).
[36] W. Wang, R. H. Hammond, M. M. Fejer, and M. R. Beasley, J. Vac. Sci. Technol., A **17**, 2676–2684 (1999).
[37] J. H. Haeni, C. D. Theis, and D. G. Schlom, J. Electroceram. **4**, 385–391 (2000).
[38] Y. Du, T. C. Droubay, A. V. Liyu, G. Li, and S. A. Chambers, Appl. Phys. Lett. **104**, 163110 (2014).
[39] Y. Du and S. A. Chambers, Appl. Phys. Lett. **105**, 163113 (2014).
[40] K. G. Günther, Naturwiss. **45**, 415–416 (1958).
[41] J. R. Arthur, Jr., J. Appl. Phys. **39**, 4032–4034 (1968).
[42] A. Y. Cho, Surf. Sci. **17**, 494–503 (1969).
[43] A. Y. Cho, J. Appl. Phys. **41**, 2780–2786 (1970).
[44] A. Y. Cho, J. Appl. Phys. **42**, 2074–2081 (1971).
[45] H. Freller and K. G. Günther, Thin Solid Films **88**, 291–307 (1982).
[46] R. Heckingbottom, G. J. Davies, and K. A. Prior, Surf. Sci. **132**, 375–389 (1983).
[47] H. Seki and A. Koukitu, J. Cryst. Growth **78**, 342–352 (1986).
[48] J. Y. Tsao, J. Cryst. Growth **110**, 595–603 (1991).
[49] J. Y. Tsao, *Materials Fundamentals of Molecular Beam Epitaxy* (Academic Press, Boston, 1993), pp. 65–88.
[50] G. Dormans, P. J. Van Veldhoven, and M. de Keijser, J. Cryst. Growth **123**, 537–544 (1992).
[51] C. D. Theis and D. G. Schlom, J. Cryst. Growth **174**, 473–479 (1997).
[52] E. H. Smith, J. F. Ihlefeld, C. A. Heikes, H. Paik, Y. Nie, C. Adamo, T. Heeg, Z. K. Liu, and D. G. Schlom, Phys. Rev. Mater. **1**, 023403 (2017).
[53] A. Prakash, P. Xu, X. Wu, G. Haugstad, X. Wang, and B. Jalan, J. Mater. Chem. C **5**, 5730–5736 (2017).
[54] MKS ASTeX model AX8401 ozone generator, MKS Instruments, Wilmington, MA, USA.
[55] R. E. Honig and D. A. Kramer, RCA Rev. **30**, 285–305 (1969).
[56] R. H. Lamoreaux, D. L. Hildenbrand, and L. Brewer, J. Phys. Chem. Ref. Data **16**, 419–443 (1987).

[57] R. Uecker, D. Klimm, R. Bertram, M. Bernhagen, I. Schulze-Jonack, M. Brützam, A. Kwasniewski, T. M. Gesing, and D. G. Schlom, Acta Phys. Pol., A **124**, 295–300 (2013).
[58] Z.-K. Liu, J. Phase Equilib. Diffus. **30**, 517–534 (2009).
[59] Y. Li, L. Zhang, Y. Ma, and D. J. Singh, APL Mater. **3**, 011102 (2015).
[60] D. Balz and K. Plieth, Z. Elektrochem. **59**, 545–551 (1955).
[61] S. N. Ruddlesden and P. Popper, Acta Crystallogr. **10**, 538–539 (1957).
[62] S. N. Ruddlesden and P. Popper, Acta Crystallogr. **11**, 54–55 (1958).
[63] R. Takahashi, K. Valset, E. Folven, E. Eberg, J. K. Grepstad, and T. Tybell, Appl. Phys. Lett. **97**, 081906 (2010).
[64] C. M. Brooks, L. Fitting Kourkoutis, T. Heeg, J. Schubert, D. A. Muller, and D. G. Schlom, Appl. Phys. Lett. **94**, 162905 (2009).
[65] R. Uecker, B. Velickov, D. Klimm, R. Bertram, M. Bernhagen, M. Rabe, M. Albrecht, R. Fornari, and D. G. Schlom, J. Cryst. Growth **310**, 2649–2658 (2008).
[66] F. G. Kinyanjui, S. T. Norberg, C. S. Knee, I. Ahmed, S. Hull, L. Buannic, I. Hung, Z. Gan, F. Blanc, C. P. Grey, and S. G. Eriksson, J. Mater. Chem. A **4**, 5088–5101 (2016).
[67] H. Kiessig, Ann. Phys. **402**, 769–788 (1931).
[68] J. B. Nelson and D. P. Riley, Proc. Phys. Soc. **57**, 160–177 (1945).
[69] J. Park, N. Tanen, H. Paik, D. Jena, and D. G. Schlom, "Hall measurement and optical properties of lightly doped La-$BaSnO_3$ films grown by molecular beam epitaxy," (unpublished).
[70] D. A. Muller, N. Nakagawa, A. Ohtomo, J. L. Grazul, and H. Y. Hwang, Nature **430**, 657–661 (2004).
[71] F. C. Frank, Acta Crystallogr. **4**, 497–501 (1951).
[72] A. Slassi, M. Hammi, and O. El Rhazouani, J. Electron. Mater. **46**, 4133–4139 (2017).
[73] T. Maekawa, K. Kurosaki, and S. Yamanaka, J. Alloys Compd. **416**, 214–217 (2006).
[74] W. Y. Wang, Y. L. Tang, Y. L. Zhu, J. Suriyaprakash, Y. B. Xu, Y. Liu, B. Gao, S. W. Cheong, and X. L. Ma, Sci. Rep. **5**, 16097 (2015).
[75] D. O. Scanlon, Phys. Rev. B **87**, 161201 (2013).
[76] L. Weston, L. Bjaalie, K. Krishnaswamy, and C. G. Van de Walle (unpublished).
[77] D. T. J. Hurle, J. Appl. Phys. **107**, 121301 (2010).

Supplementary Material

Adsorption-controlled growth of La-doped $BaSnO_3$ by molecular-beam epitaxy

Hanjong Paik,[1] Zhen Chen,[2] Edward Lochocki,[3] Ariel Seidner H.,[1] Amit Verma,[4] Nicholas Tanen,[1,5] Jisung Park,[1] Masaki Uchida,[6] ShunLi Shang,[7] Bi-Cheng Zhou,[7] Mario Brützam,[8] Reinhard Uecker,[8] Zi-Kui Liu,[7] Debdeep Jena,[1,5] Kyle M. Shen,[3,9] David A. Muller,[2,9] and Darrell G. Schlom[1,9,a]

[1] Department of Material Science and Engineering, Cornell University, Ithaca, New York 14853, USA

[2] School of Applied and Engineering Physics, Cornell University, Ithaca, New York 14853, USA

[3] Laboratory of Atomic and Solid State Physics, Department of Physics, Cornell University, Ithaca, New York 14853, USA

[4] Department of Electrical Engineering, IIT Kanpur, Kanpur 208016, India

[5] School of Electrical and Computer Engineering, Cornell University, Ithaca, New York 14853, USA

[6] Department of Applied Physics and Quantum-Phase Electronics Center (QPEC), University of Tokyo, Tokyo 113-8656, Japan

[7] Department of Materials Science and Engineering, The Pennsylvania State University, University Park, Pennsylvania 16802, USA

[8] Leibniz Institute for Crystal Growth, D-12489 Berlin, Germany

[9] Kavli Institute at Cornell for Nanoscale Science, Ithaca, New York 14853, USA

S1 Calculated partial pressure of the species in the gas phase over solid SnO_2 as a function of temperature at a fixed oxygen partial pressure of 7.6×10^{-7} Torr (10^{-9} atm)

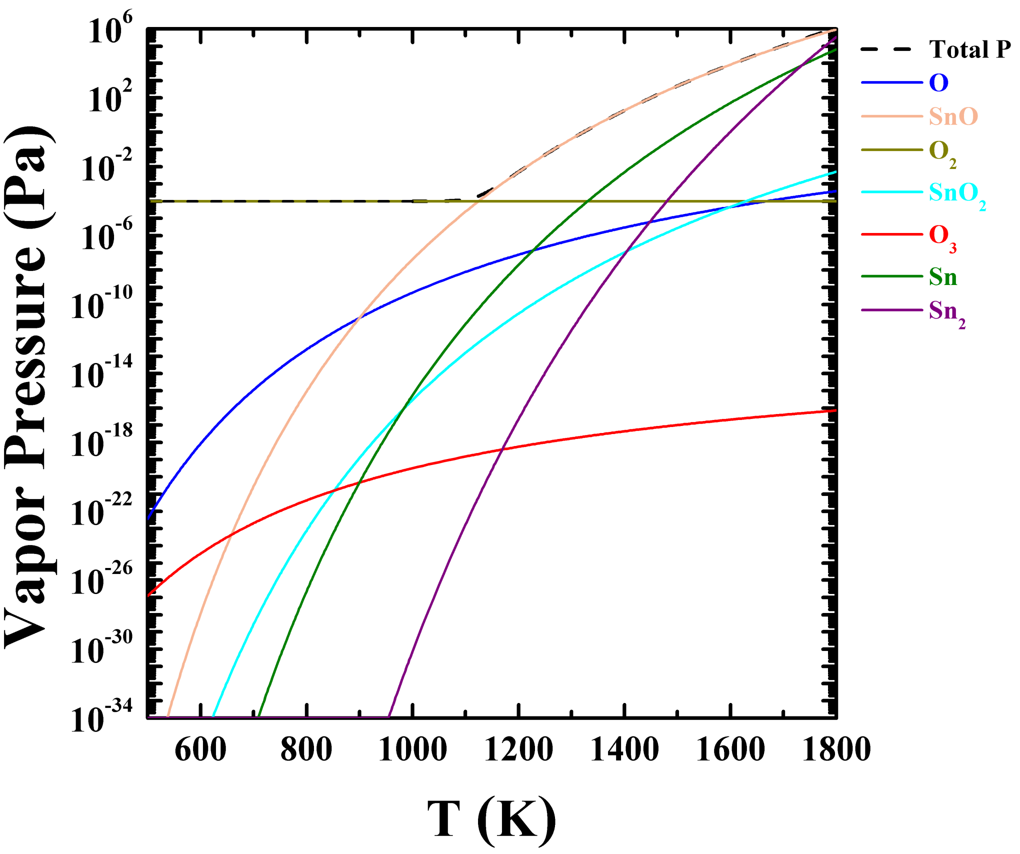

Figure S1: Calculated partial pressure of the species in the gas phase over solid SnO_2 as a function of temperature at a fixed oxygen partial pressure of 7.6×10^{-7} Torr (10^{-9} atm).

S2 CALPHAD method and first-principles calculation of *P-T* phase diagram of the Ba-Sn-O system

Enthalpies of formation of $Ba_{n+1}Sn_nO_{3n+1}$ (n=1, 2, and 3) from first-principles calculations at 0 K together with thermodynamic data in the SSUB database[S1] were used in the CALPHAD calculations of the Ba-Sn-O phase diagram. The formation enthalpies of relevant phases are listed in Table S1. The reactions to form and the predicted reaction enthalpies of $Ba_{n+1}Sn_nO_{3n+1}$ at 0 K are shown in Table I. There was a report on the predicted enthalpies of formation of $Ba_{n+1}Sn_nO_{3n+1}$.[S2] We believe that present enthalpies of formation are more accurate due to the adopted exchange-correction functional of PBEsol according to our tests.

All these first-principles results indicate that the driving forces to form $Ba_{n+1}Sn_nO_{3n+1}$ with $n>2$ are small. Hence, the phases of $Ba_{n+1}Sn_nO_{3n+1}$ with $n>2$ are not shown in the P-T phase diagram of Fig. 1 according to the present first-principles data at 0 K. At high temperatures and if the entropy contribution included, $Ba_{n+1}Sn_nO_{3n+1}$ phases with $n>2$ may become stable and those that are should appear in region **II** of Fig. 1. This case is, however, beyond the scope of the present work.

First-principles calculations were performed using the generalized gradient approximation (GGA) with the PBEsol functional[S3] as implemented in the *Vienna Ab initio Simulation Package* (VASP 5.4.1).[S4,S5] We used the standard projector augmented wave (PAW) potentials[S6] provided by VASP. The core configurations for each element were: Ba ($5s^25p^66s^2$), Sn ($5s^25p^2$), and O ($2s^22p^4$). An energy cut-off of 520 eV was used for all of the calculations. The Monkhorst–Pack *k*-point grids for Brillouin zone sampling were used in all of the structural relaxations and subsequent static calculations. The *k*-point configurations used in each structure were: 10×10×10 (BaO), 10×10×10 (SnO_2), 10×10×10 ($BaSnO_3$), and 10×10×4 (Ba_2SnO_4).

Table S1: Enthalpy of formation of relevant Ba-Sn-O phases (at 0 K) calculated by first-principles methods.

	Total energy (eV/atom)	
Phases	**Materials Project[S7] using PBE**	**Current work using PBEsol**
BaO	–5.9136	–6.2003
SnO_2	–6.2835	–6.6116
$BaSnO_3$	–6.3288	–6.6700
Ba_2SnO_4	–6.2805	–6.6049
$Ba_3Sn_2O_7$	–6.3022	–6.6326
$Ba_4Sn_3O_{10}$	–6.3038	–6.6432

S3 X-ray diffraction results corresponding to the RHEED patterns in the *P-T* diagram shown in Fig. 1

Region **II** in Fig. 1—Ba-rich $BaSnO_3$

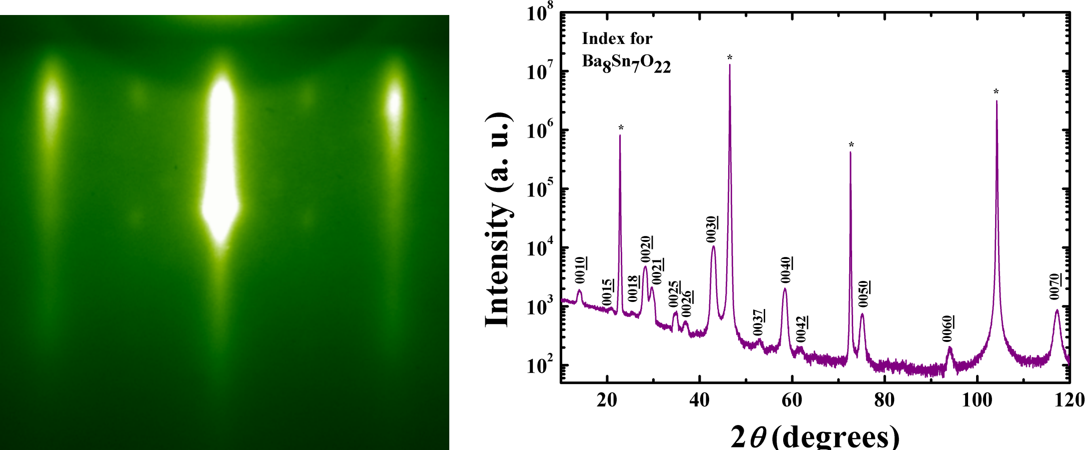

Figure S2: A θ-2θ XRD scan over a wider region reveals RP phase peaks. It can be indexed as $Ba_8Sn_7O_{22}$ ($Ba_{n+1}Sn_nO_{3n+1}$, n=7) with both even an odd 00ℓ peaks due to the presence of significant layering disorder similar to $Sr_{n+1}Ti_nO_{3n+1}$.[S8]

Region between **II** and **III** in Fig. 1—slightly Ba-rich $BaSnO_3$

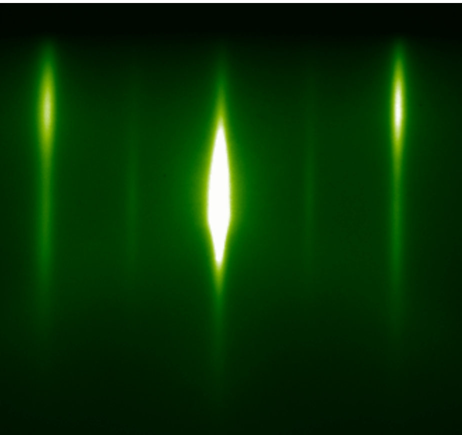

Figure S3: When the $BaSnO_3$ film growth conditions become slightly Ba-rich by either increasing the substrate temperature or lowering the flux supplied from the SnO_2 source, the 2×1 reconstruction RHEED pattern appeared along the [110] azimuth of $BaSnO_3$.

Region **III** in Fig. 1—stoichiometric $BaSnO_3$

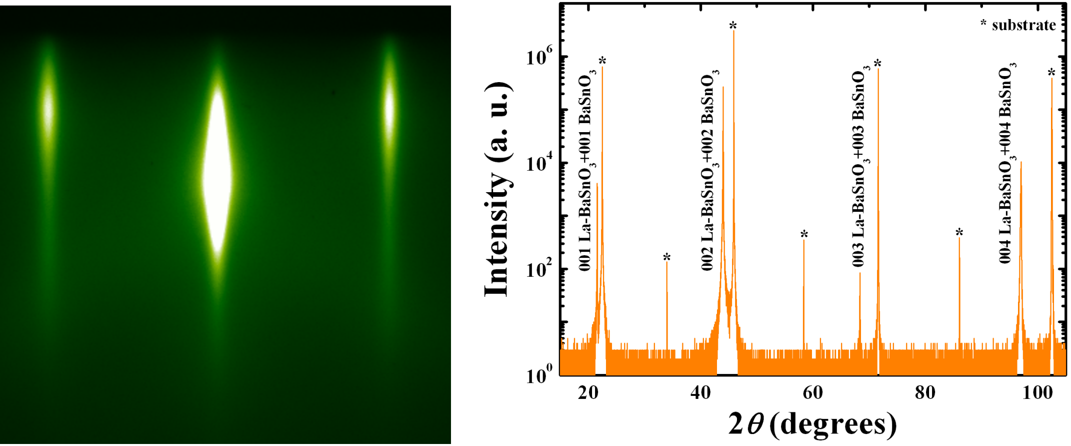

Figure S4: Stoichiometric $BaSnO_3$ films grow with a 1×1 RHEED pattern along the [110] azimuth of $BaSnO_3$.

Region **IV** in Fig. 1—Sn-rich $BaSnO_3$

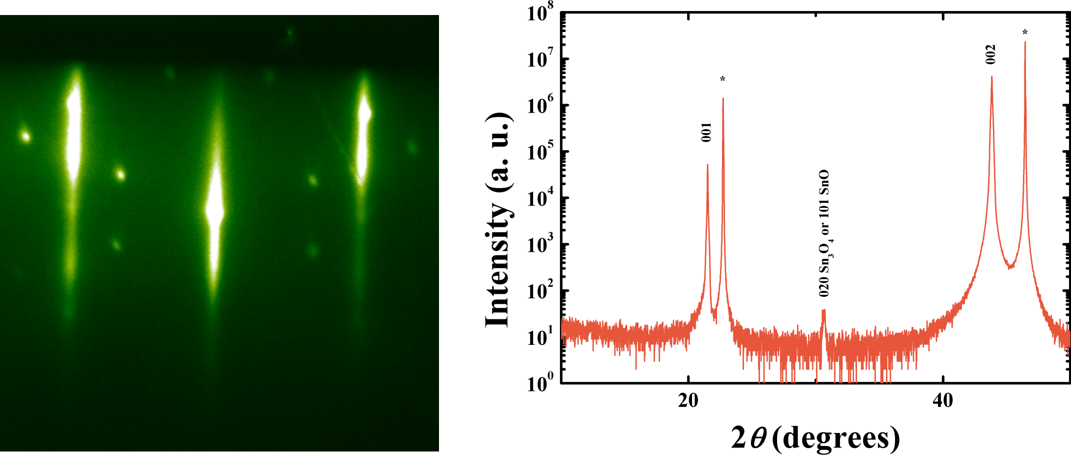

Figure S5: The rough SnO_2 phase gives rise to the spots in the resulting RHEED pattern; the streaks are from the perovskite $BaSnO_3$ phase. The resulting mixed-phase sample of SnO_2+$BaSnO_3$ is shown in XRD.

S4 Atomic force microscope image of the highest mobility La-$BaSnO_3$ thin film

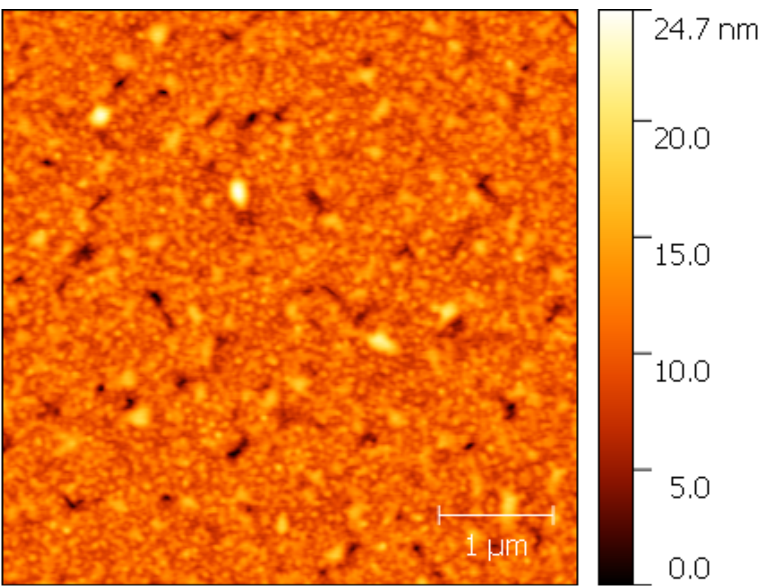

Figure S6: Atomic force microscope image of the surface of a 60 nm thick La-doped $BaSnO_3$ film with a mobile carrier concentration of 1.2×10^{20} cm^{-3} grown on a 330 nm thick undoped $BaSnO_3$ buffer layer on a (001) $DyScO_3$ substrate. This is the same high-mobility sample characterized in Figs. 2-6.

S5 Edge dislocations with Burgers vector ½ *a* <110> and *a* <110>

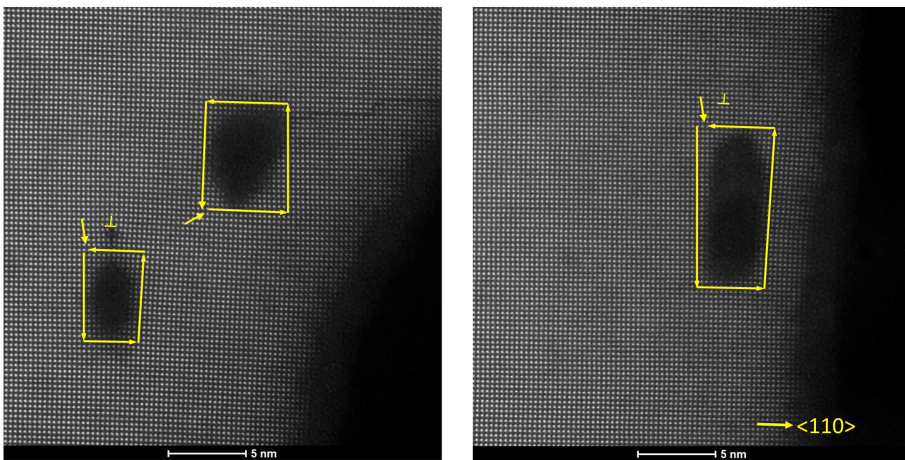

Figure S7: Plan-view HAADF-STEM images of the same high-mobility sample characterized in Figs. 2-6 and S6. Four dislocations are present in this pair of images. The Burgers circuit is drawn around three of them, revealing two partial edge dislocations in the image on the left, each with a Burgers vector with an in-plane projection of ½ ***a*** <110>. In contrast, the image on the right contains a Burgers vector with an in-plane projection of ***a*** <110>. The yellow arrows point to the lack of closure of the Burgers circuit, which is the in-plane component of each Burgers vector. The cores of all four of the dislocations in these images are hollow. Being devoid of atoms, the hollow cores appear black in these images.

S6 Stacking faults

We looked at three different images with a total area of 3.12×10^4 nm^2 and only observed one loop-shaped stacking fault. This indicates that the loop-shaped stacking fault density has an upper bound of 3×10^9 cm^{-2}. This is about two orders of magnitude lower than the stacking fault density reported by Wang *et al.*[S9] in their epitaxial $BaSnO_3$ films.

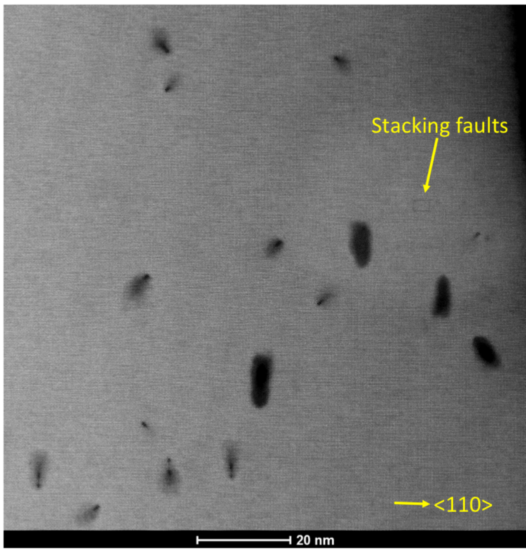

Figure S8: Low-magnification, plan-view HAADF-STEM image of the same high-mobility sample characterized in Figs. 2-6, S6, and S7. A single loop-shaped stacking fault is indicated by the yellow arrow.

S7 STEM-EELS

Using electron energy loss spectroscopy within a scanning transmission electron microscope (STEM-EELS) we assessed the oxidation state of the tin in the same La-doped $BaSnO_3$ sample that has the highest mobility. The results are shown in Fig. S9. The two peaks indicated by the arrows in the measured Sn-$M_{4,5}$ EELS edges (shown in black in Fig. S9(a)) match very well with the EELS Sn-$M_{4,5}$ edges of Sn^{4+} in SnO_2 (shown in green in Fig. S9(a)).[S10] The Sn-$M_{4,5}$ edges from Sn^{2+} in SnO (shown in red in Fig. S9(a)) exhibit significantly different peaks.[S10] This shows that the tin in this high mobility La-doped $BaSnO_3$ film mainly has a valence state of 4+. Furthermore, the O-K spectra measured on this same film (shown in black in Fig. S9(b)) also agrees well with that from a $BaSnO_3$ film grown in an adsorption-controlled regime by MBE utilizing metalorganic precursors on $SrTiO_3$ (shown in green in Fig. S9(b))[S11] as well as the simulated O-K edge of a $BaSnO_3$ single crystal (shown in red in Fig. S9(b)).[S11]

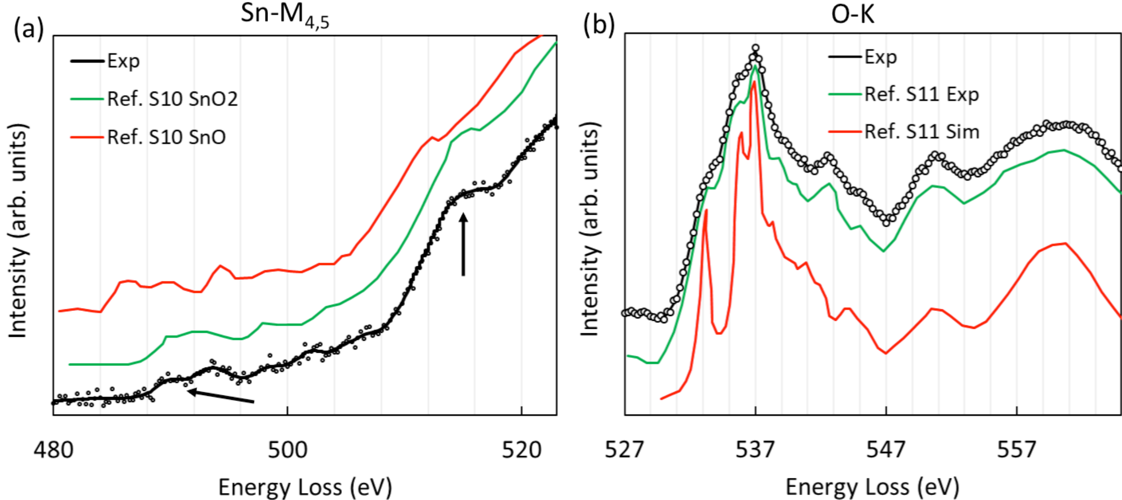

Figure S9: STEM-EELS spectra of the same high-mobility sample characterized in Figs. 2-6 and S6-S8. In (a) the Sn-$M_{4,5}$ EELS spectra of the La-doped $BaSnO_3$ film (black) are compared with the Sn-$M_{4,5}$ EELS spectra of SnO_2 (green) and SnO (red) from Ref. S10. Agreement between the $BaSnO_3$ and SnO_2 spectra, i.e., Sn^{4+}, is evident; see in particular the arrowed features. In (b) the O-K EELS spectra of the same La-doped $BaSnO_3$ film (black) are compared with O-K EELS spectra from a $BaSnO_3$ film grown by MBE utilizing metalorganic precursors on $SrTiO_3$ (green) from Ref. S11 and a simulated EELS spectrum of $BaSnO_3$ also from Ref. S11. Agreement among the $BaSnO_3$ spectra in (b) is evident.

Supplemental References

S1. Scientific Group Thermodata Europe (SGTE), Thermodynamic Properties of Inorganic Materials. In *Landolt-Boernstein New Series, Group IV*, Lehrstuhl fuer Theoretische Huettenkunde, Ed. Springer: Verlag Berlin Heidelberg, 1999; Vol. 19.

S2. Y. Li, L. Zhang, Y. Ma, and D. J. Singh, APL Mater. **3**, 011102 (2015)

S3. J. P. Perdew, A. Ruzsinszky, G. I. Csonka, O. A. Vydrov, G. E. Scuseria, L. A. Constantin, X. Zhou, and K. Burke, Phys. Rev. Lett. **100**, 136406 (2008).

S4. G. Kresse, J. Furthmüller, Phys. Rev. B Condens. Matter. **54**, 11169–11186 (1996).

S5. G. Kresse, J. Hafner, Phys. Rev. B **47**, 558–561 (1993).

S6. P. E. Blöchl, Phys. Rev. B **50**, 17953–17979 (1994).

S7. A. Jain, S. P. Ong, G. Hautier, W. Chen, W. D. Richards, S. Dacek, S. Cholia, D. Gunter, D. Skinner, G. Ceder, and K. A. Persson, APL Mater. **1**, 011002 (2013).

S8. C. M. Brooks, R. B. Wilson, A. Schäfer, J. A. Mundy, M. E. Holtz, D. A. Muller, J.Schubert, D. G. Cahill, and Darrell G. Schlom, Appl. Phys. Lett. **107**, 051902 (2015).

S9. W. Y. Wang, Y. L. Tang, Y. L. Zhu, J. Suriyaprakash, Y. B. Xu, Y. Liu, B. Gao, S. W. Cheong, and X. L. Ma, Sci. Rep. **5**, 16097 (2015).

S10. See Fig. 1 in M.S. Moreno, R.F. Egerton, and P.A. Midgley, Phys. Rev. B **69**, 233304 (2004).

S11. H. Yun, M. Topsakal, A. Prakash, K. Ganguly, C. Leighton, B. Jalan, R. M Wentzcovitch, K. A. Mkhoyan, and J. S. Jeong, arXiv:1611.09284.